

Photoproduction of $\pi^0\omega$ off protons for $E_\gamma \leq 3$ GeV

The CB-ELSA Collaboration

J. Junkersfeld¹, A.V. Anisovich^{1,2}, G. Anton³, R. Bantes⁴, O. Bartholomy¹, R. Beck¹, Yu. Beloglazov², R. Bogendörfer³, R. Castelijns^{5,a}, V. Crede^{1,6}, A. Ehmanns¹, J. Ernst¹, I. Fabry¹, H. Flemming^{8,b}, A. Fösel³, M. Fuchs¹, Ch. Funke¹, R. Gothe^{4,c}, A. Gridnev², E. Gutz¹, St. Höffgen⁴, I. Horn¹, J. Höbl³, H. Kalinowsky¹, F. Klein⁴, E. Klempt¹, H. Koch⁸, M. Konrad⁴, B. Kopf⁸, B. Krusche⁹, J. Langheinrich^{4,c}, H. Löhner⁵, I. Lopatin², J. Lotz¹, H. Matthäy⁸, D. Menze⁴, J. Messchendorp^{7,d}, V.A. Nikonov^{1,2}, D. Novinski², M. Ostrick^{4,e}, A. Radkov², A.V. Sarantsev^{1,2}, S. Schadmand^{7,a}, C. Schmidt¹, H. Schmieden⁴, B. Schoch⁴, G. Suft³, V. Sumachev², T. Szczepanek¹, H. van Pee^{1,7}, U. Thoma^{1,7}, D. Walther⁴, and Ch. Weinheimer^{1,f}

¹ Helmholtz-Institut für Strahlen- und Kernphysik, Universität Bonn, Germany

² Petersburg Nuclear Physics Institute, Gatchina, Russia

³ Physikalisches Institut, Universität Erlangen, Germany

⁴ Physikalisches Institut, Universität Bonn, Germany

⁵ Kernfysisch Versneller Instituut, Groningen, The Netherlands

⁶ Department of Physics, Florida State University, Tallahassee, FL, USA

⁷ II. Physikalisches Institut, Universität Gießen, Germany

⁸ Institut für Experimentalphysik I, Universität Bochum, Germany

⁹ Institut für Physik, Universität Basel, Switzerland

^a Present address: Institut für Kernphysik, Forschungszentrum Jülich, Germany

^b Present address: GSI, Darmstadt, Germany

^c Present address: University of South Carolina, Columbia, SC, USA

^d Present address: Kernfysisch Versneller Instituut, Groningen, The Netherlands

^e Present address: Institut für Kernphysik, Universität Mainz, Germany

^f Present address: Institut für Kernphysik, Universität Münster, Germany

Received: August 15, 2019/ Revised version:

Abstract. Differential and total cross-sections for photoproduction of $\gamma p \rightarrow p\pi^0\omega$ and $\gamma p \rightarrow \Delta^+\omega$ were determined from measurements of the CB-ELSA experiment, performed at the electron accelerator ELSA in Bonn. The measurements covered the photon energy range from the production threshold up to 3 GeV.

PACS. 13.30.-a Decays of baryons – 13.60.Le Meson production – 14.20.Gk Baryon resonances with S=0

1 Introduction

A large number of baryon resonances has been established experimentally [1]. Below a mass of $1.8 \text{ GeV}/c^2$, most of these states are well reproduced by constituent quark models [2,3,4]. The models differ in details of the predicted mass spectrum but have a common feature: above $1.8 \text{ GeV}/c^2$, they predict many more states than have been seen experimentally. A natural explanation for these *missing resonances* is that they have escaped detection. The majority of known non-strange baryon resonances stems from πN scattering experiments. Model calculations show that for some of these missing resonances only a small coupling to πN is expected [5]. In elastic scattering, the coupling to πN enters in the entrance and exit channel so

these resonances contribute only very weakly. By contrast, these resonances are predicted to have normal photo couplings [6] and some of them should be observed in channels like $N\eta$, $K\Lambda$, $K\Sigma$ [7], $\Delta\eta$ or $\Delta\omega$ [8]. In comparison to the $N\pi$ final state, most of the above provide a distinctive advantage: they act as isospin filters; only N^* resonances contribute to the $N\eta$ and $K\Lambda$ final states while resonances in $\Delta\eta$, and $\Delta\omega$ belong to the Δ^* series.

A partial-wave analysis of various photoproduction data suggested the existence of several new resonances [9]. The analysis included data from CB-ELSA on π^0 and η photoproduction [10,11], Mainz-TAPS data on η photoproduction [12], beam-asymmetry measurements of π^0 and η [13,14,15], data on $\gamma p \rightarrow n\pi^+$ [16] and from the compilation of the SAID database [17], and data on photoproduction

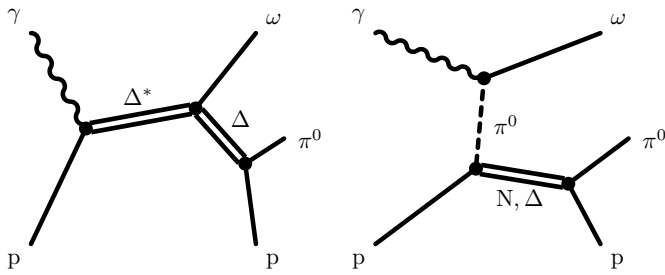


Fig. 1. Contributions to $\Delta\omega$ photoproduction: left, production of Δ^* intermediate states; right: production of ω mesons via t -channel pion exchange.

of $\gamma p \rightarrow K^+\Lambda$ and $\gamma p \rightarrow K^+\Sigma^0$ from SAPHIR [18,19], CLAS [20,21], and LEPS [22].

The reaction $\gamma p \rightarrow p\omega$ is known to receive large contributions from t -channel exchange processes [23,24]. A similar mechanism may contribute also to $\Delta\omega$ photoproduction: the incoming photon may couple to $\omega\pi^0$, the virtual π^0 excites the nucleon to a Δ and the ω escapes, preferentially in forward direction. Fig. 1 shows a Feynman diagram for this reaction mechanism and for the production of a Δ resonance decaying into $\Delta\omega$.

This paper reports on a measurement of differential and total cross sections for the reaction

$$\gamma p \rightarrow p\pi^0\omega, \quad (1)$$

with $\omega \rightarrow \pi^0\gamma$ and the π^0 detected in its two photon decay. From this data the total cross-section for

$$\gamma p \rightarrow \Delta^+\omega \quad (2)$$

with the subsequent decays

$$\Delta^+ \rightarrow p\pi^0 \quad \text{and} \quad \omega \rightarrow \pi^0\gamma$$

was extracted and compared to an earlier measurement at higher energies [25]. The low statistics for reactions (1) and (2) does not yet provide a sufficiently large data sample for a partial-wave analysis, but may serve as a guide for what to expect from future experiments and is thus of exploratory character.

2 Experimental setup

The experiment was performed at the Electron Stretcher Accelerator ELSA [26] at the University of Bonn. Electrons were extracted at an energy of 3.2 GeV and bremsstrahlung was produced in a radiator foil with a thickness of 3/1000 of a radiation length (Fig. 2). Electrons deflected in a magnet were detected with a tagging system covering the photon energy range from 750 to 2970 MeV. The tagging system consisted of 14 thick scintillation counters and two proportional wire chambers with a total of 352 wires. The scintillation counters were used to derive a fast timing signal and the wire chambers to determine the photon energy. The γ energy resolution varied from 30 MeV

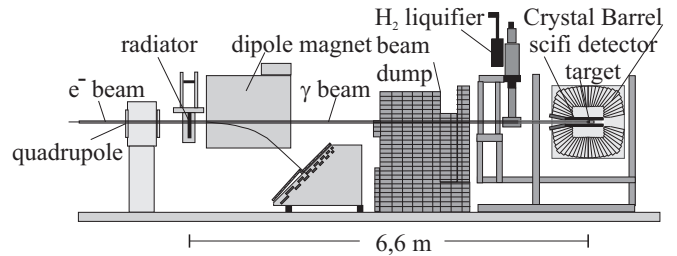


Fig. 2. Setup of the CB-ELSA experiment

at the lower end to 0.5 MeV at the upper end of the spectrum not taking into account the energy distribution of the electron beam of 3 – 5 MeV [26]. This is well matched with the overall resolution of the detector for this reaction of 30 MeV (FWHM) (see below). Typical rates were $1 - 3 \times 10^6$ photons/s. The photon beam hit a liquid H_2 target of 5.3 cm length and 3 cm diameter. The absolute normalisation was derived from a comparison of our differential angular distributions for the reaction $\gamma p \rightarrow p\pi^0$ with the SAID model SM02. The normalisation uncertainty was estimated to be 15 % [10,27].

Charged reaction products were detected by a three-layer scintillating fibre detector covering polar angles from 15° to 165° [28]. The outer layer was parallel to the beam axis, the fibres of the other two layers were bent $\pm 25^\circ$ with respect to the first layer to allow for a spatial reconstruction of hits. Photons and charged particles were detected in the Crystal Barrel detector [29], a calorimeter consisting of 1380 CsI(Tl) crystals with photodiode read-out, covering 98 % of 4π solid angle. The detector with its high granularity and energy resolution is excellently suited for the detection of multi-photon final states.

Electromagnetic showers typically extended over up to 30 crystals in the calorimeter. Photons were reconstructed with an energy resolution of $\sigma_E/E = 2.5\%/\sqrt{E[\text{GeV}]}$ and an angular resolution of $\sigma_{\theta,\phi} \approx 1.1^\circ$. Hits due to charged particles induce smaller clusters with typical 3 – 6 crystals.

A fast first-level trigger signal was derived from a coincidence between a hit in the tagging system and a signal in at least two out of three layers of the inner fibre detector. The second-level trigger required a minimum number of hits in the calorimeter. For part of the data the minimal number of hits in the calorimeter was 2, otherwise at least 3 hits were requested, in order to reduce the dead-time. Dead-time losses were below 70 %, and below 20 % for the more restrictive trigger.

A more detailed description of the experimental setup and the event reconstruction can be found in [27].

3 The reaction $\gamma p \rightarrow p\pi^0\omega$

3.1 Event selection

The reaction $\gamma p \rightarrow p\pi^0\omega$, $\omega \rightarrow \pi^0\gamma$, leads to a final state with five photons and a proton. The $\pi^0\omega$ photoproduction threshold is at $E_\gamma = 1365$ MeV; a cut on a tagged photon energy $E_\gamma > 1315$ MeV was applied right at the beginning.

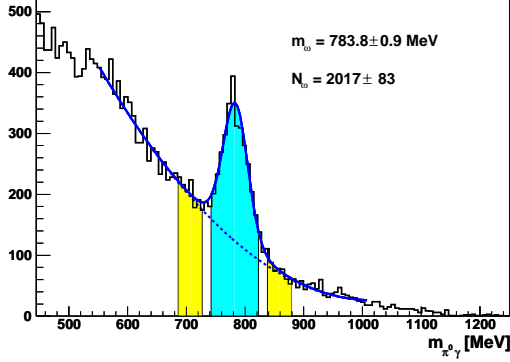


Fig. 3. ω signal in $\pi^0\gamma$ invariant mass

The first step in the analysis is the identification of the five photons and the reconstruction of their energies and directions. Protons with E_{kin} below ~ 95 MeV only produce a signal in the inner detector but not in the calorimeter. Hence in the analysis, events were selected with 5 or 6 hits in the Crystal Barrel calorimeter and 1 – 3 hits in the inner detector. (A three-hit pattern can arise from three single hits in each layer not crossing in a single point.) At least two layers of the inner detector had to have a signal. For each pair of fibre and barrel hits it was tested if the two vectors pointing from the target centre to a fibre-detector-hit and to a Crystal-Barrel-hit form an angle of 20° or less; in this case the Crystal Barrel hit was identified as a proton, otherwise as a photon. The 20° matching angle was chosen to allow for the extension of the target and the uncertainties in the measurement. Events with five photons were kept for further analysis. In case of 6 hits in the barrel, one of them had to match the proton identification.

Surviving events were kinematically fitted to the hypothesis $\gamma p \rightarrow p_{\text{miss}} \pi^0 \pi^0 \gamma$ with a missing proton, neglecting identified charged hits and using all remaining photon candidates. The kinematic fit assumed that the reaction took place in the target centre. Since the momentum of the proton is unknown and needs to be reconstructed, energy and momentum conservation give one constraint, the π^0 masses two constraints. A cut on a confidence level of 2% was applied, optimised to lose only few good events. From the fit, the flight direction of the proton was determined and compared to hits in the inner detector. Again, the direction of the missing proton and the direction to a hit in the inner fibre detector had to form an angle of $\pm 20^\circ$ or less for the hit to be identified as proton.

The $p\pi^0\pi^0\gamma$ events were used to identify $p\pi^0\omega$ events with ω decaying into $\pi^0\gamma$. Fig. 3 shows the $\pi^0\gamma$ mass distribution with two entries per event. The fit using a Voigt function (a Breit-Wigner convoluted with a Gaussian) imposing the ω width of $\Gamma = 8.49 \text{ MeV}/c^2$ assigns about 2000 events to reaction (1). The ω mass was determined to $(783.8 \pm 0.9_{\text{stat}} \pm 1.0_{\text{syst}}) \text{ MeV}/c^2$. The systematic error was estimated from the comparison of η, η' , and ω masses in different reactions with the PDG values. The mass resolution is determined to $\sigma = 16 \text{ MeV}/c^2$.

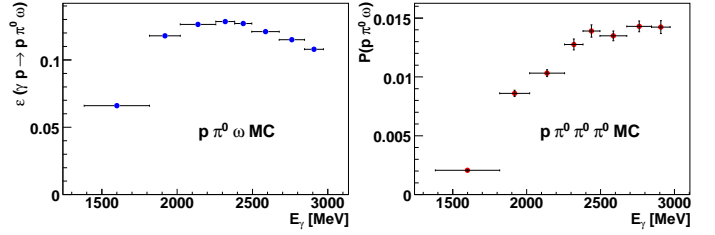


Fig. 4. Acceptance of $p\pi^0\omega$ events (left) and the misidentification probability of $p3\pi^0$ events (right).

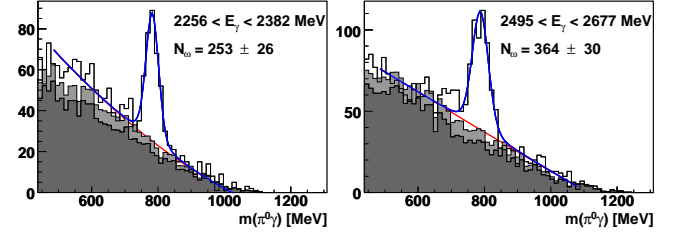


Fig. 5. The ω signal with background. The background is predicted in height and shape by simulations of $p3\pi^0$ (dark-grey) and $p\pi^0\omega$ combinatorial background (light-grey).

The background in the $\pi^0\gamma$ distribution of $p\pi^0\pi^0\gamma$ events has two main sources. A large fraction stems from $p3\pi^0$ events. Fig. 4 shows that, in the energy region $2000 < E_\gamma < 3000$ MeV, $p3\pi^0$ events have a high probability to be misidentified as $p\pi^0\omega$. The misidentification probability is only one order of magnitude smaller than the acceptance for $p\pi^0\omega$. However, the branching ratio of $p3\pi^0 \rightarrow p6\gamma$ is $(96.44 \pm 0.09)\%$ compared with $(8.71 \pm 0.25)\%$ for $p\pi^0\omega \rightarrow p5\gamma$. The cross-section for $3\pi^0$ photoproduction was estimated using the cross-section for $\gamma p \rightarrow p\eta$ [11], which was determined from events with the η decaying into $\gamma\gamma$ and $3\pi^0$. The fractions of η and non- η events in the $3\pi^0$ event samples were determined and used to estimate the cross-section of $\gamma p \rightarrow p3\pi^0$. Monte Carlo simulations were performed using the $p3\pi^0$ cross-section estimate to determine the expected number of $p3\pi^0$ events surviving the $p\pi^0\pi^0\gamma$ reconstruction. Fig. 5 shows for two photon energy ranges the predicted contribution of $p\pi^0\pi^0\pi^0$ events to the background and the observed $\pi^0\gamma$ distribution.

The expected combinatorial background was determined from the number of reconstructed $p\pi^0\omega$ events. It is shown together with the $p3\pi^0$ part of the background in Fig. 5. In the ω mass region, there is good agreement between the simulated background distribution and the observed background. The study of simulated $p\pi^0\pi^0$ and $p\pi^0\eta$ events shows misidentification probabilities of the order of 0.1%. Their contributions were neglected.

The number of events due to reaction (1) in a given energy range was determined by fitting the $\pi^0\gamma$ distribution using a Voigt function for the ω signal and a second order polynomial for the background. The fit also returned the number of background events below the peak. For background subtraction, data histograms were filled with events within the ω mass region ($m_\omega \pm 40 \text{ MeV}/c^2$) and background histograms with events falling into the upper or lower sidebands ($687 - 727 \text{ MeV}/c^2$ and $839 -$

879 MeV/c², also shown in Fig. 3). The latter histograms were scaled to contain the same number of events as found in the background below the peak. For each energy and angular region, the sideband histograms were subtracted from the data histograms to extract the $p\pi^0\omega$ distributions. The same procedure was used to determine the $p\pi^0\omega$ distributions for each energy region as function of the momentum transfer and the invariant mass respectively.

The acceptance was studied with a GEANT-based Monte Carlo simulation using phase space distributed $p\pi^0\omega$ and $\Delta^+\omega$ events. In the first iteration only $p\pi^0\omega$ Monte-Carlo events were taken into account. cross-sections for $\gamma p \rightarrow p\pi^0\omega$ and $\gamma p \rightarrow \Delta^+\omega$ were thus obtained, as will be described in sections 3.3 and 3.4, and used to produce Monte Carlo events with a realistic mixture of $p\pi^0\omega$ and $\Delta^+\omega$ events. This provides a more realistic acceptance simulation. Stable results were achieved in the second iteration. The simulated acceptance was different when only events due to phase-space distributed $p\pi^0\omega$ events or $\Delta^+\omega$ events were used for the simulation. The difference in the acceptance was taken as a contribution to the systematic error.

3.2 Differential cross-sections

The differential cross-sections were obtained from the sideband subtracted histograms. We give in the centre of mass system cross-sections differential in $\cos\theta_\omega$, $\cos\theta_{\pi^0}$ and $|t - t_{\min}|$,

$$d\sigma/d\Omega(\cos\theta_\omega), \quad d\sigma/d\Omega(\cos\theta_{\pi^0}), \quad d\sigma/dt(|t - t_{\min}|),$$

respectively. Here t is the squared four-momentum transfer from the photon beam to the $p\pi^0$ system given by

$$t = q^2 = (p_\gamma - p_\omega)^2 \quad (3)$$

and t_{\min} is the minimal momentum transfer imposed by kinematics.

Fig. 6 presents the differential cross-sections as a function of $\cos\theta_\omega$, in table they are given in numerical form. The distributions are compatible with a description of the form

$$\frac{d\sigma}{d\Omega}(x) = a_0 + a_1 \cdot e^{a_2 x} \quad \text{with } x = \cos\theta. \quad (4)$$

In the backward direction, the acceptance is small and the errors large. The fit using Eq. (4) took into account only data for which the acceptance ϵ was above 5% (thus restricting the fit range to $\cos\theta_\omega > -0.6$ for $E_\gamma < 1800$ MeV, and to $\cos\theta_\omega > -0.8$ for $E_\gamma > 1800$ MeV), and was then extrapolated to cover the full $\cos\theta_\omega$ range. In the forward direction, there is a strong increase in intensity, in particular at energies above 2 GeV. Production of ω mesons via t -channel exchange with simultaneous $p \rightarrow \Delta(1232)$ excitation seems to play an important role in the dynamics of reaction (1).

From the $\cos\theta_\omega$ distributions a total cross-section was determined by summing over the measured values for which the acceptance was above 5% and using extrapolated values in the remaining range.

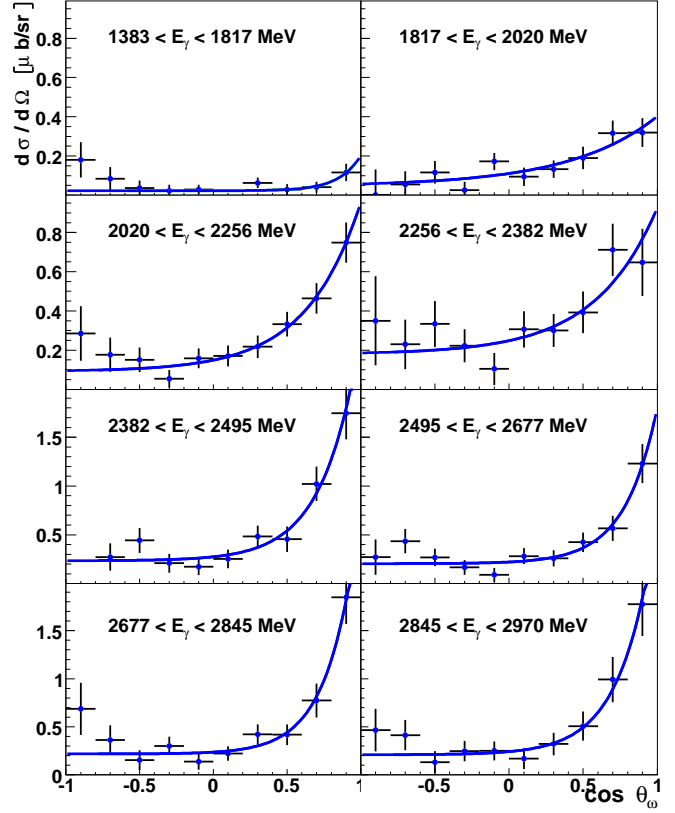


Fig. 6. Differential cross-sections $d\sigma/d\Omega(\cos\theta_\omega)$.

The differential cross-sections $d\sigma/d\Omega(\cos\theta_{\pi^0})$ are shown in Fig. 7 and listed numerically in 2. There are no obvious structures beside some fluctuations in the forward and backward regions. The data were fitted using a constant. The fit was restricted to data points measured with an acceptance of at least 5%, thus excluding for $E_\gamma > 2380$ MeV the points with $\cos\theta_{\pi^0} > 0.8$. From this distribution the total cross-section is derived from the data points and the extrapolation was used for the points with small acceptance.

Fig. 8 shows the differential cross-sections $d\sigma/dt$ in dependence of $|t - t_{\min}|$, which are compatible with an exponential behaviour in the low t region. This is characteristic for production via t -channel exchange. The data were fitted in the region below $0.8 \cdot |t_{\max} - t_{\min}|$ (approximately corresponding to $\epsilon > 5\%$) using

$$\frac{d\sigma}{dt}(|t - t_{\min}|) = e^{a+b|t-t_{\min}|} + c(E) \quad (5)$$

where t_{\min} is the minimum squared momentum transfer imposed by kinematics. The non- t -dependent contribution was described with a function $c(E) = c_0 + c_1 \cdot E_\gamma$. The parameters c_0 and c_1 were determined in a combined fit of the differential cross sections.

The slope parameter b is shown in Fig. 9. The slope is approximately constant over the covered energy range. This indicates a strong contribution from ω production via t -channel exchange processes.

Table 1. Differential cross-sections $d\sigma/d\Omega(\cos\theta_\omega)$. There is a common systematic error of 16 %.

$\cos\theta_\omega$	$d\sigma/d\Omega(\cos\theta_\omega)$ [$\mu\text{b}/\text{sr}$]	$d\sigma/d\Omega(\cos\theta_\omega)$ [$\mu\text{b}/\text{sr}$]	$d\sigma/d\Omega(\cos\theta_\omega)$ [$\mu\text{b}/\text{sr}$]	$d\sigma/d\Omega(\cos\theta_\omega)$ [$\mu\text{b}/\text{sr}$]
E_γ [MeV]	1383 - 1817	1817 - 2020	2020 - 2256	2256 - 2382
-1.00 - -0.80	0.16 ± 0.08	0.00 ± 0.13	0.29 ± 0.14	0.35 ± 0.23
-0.80 - -0.60	0.08 ± 0.06	0.05 ± 0.07	0.18 ± 0.09	0.23 ± 0.13
-0.60 - -0.40	0.04 ± 0.04	0.12 ± 0.06	0.15 ± 0.06	0.33 ± 0.12
-0.40 - -0.20	0.02 ± 0.03	0.03 ± 0.04	0.05 ± 0.04	0.22 ± 0.08
-0.20 - 0.00	0.03 ± 0.02	0.17 ± 0.04	0.16 ± 0.05	0.10 ± 0.08
0.00 - 0.20	-0.02 ± 0.02	0.09 ± 0.05	0.17 ± 0.05	0.31 ± 0.09
0.20 - 0.40	0.06 ± 0.03	0.13 ± 0.04	0.22 ± 0.06	0.30 ± 0.08
0.40 - 0.60	0.03 ± 0.03	0.19 ± 0.06	0.33 ± 0.06	0.39 ± 0.11
0.60 - 0.80	0.04 ± 0.03	0.32 ± 0.06	0.46 ± 0.08	0.71 ± 0.13
0.80 - 1.00	0.11 ± 0.04	0.32 ± 0.07	0.75 ± 0.10	0.65 ± 0.17
E_γ [MeV]	2382 - 2495	2495 - 2677	2677 - 2845	2845 - 2970
-1.00 - -0.80	-0.10 ± 0.25	0.27 ± 0.18	0.70 ± 0.28	0.47 ± 0.23
-0.80 - -0.60	0.27 ± 0.14	0.44 ± 0.13	0.37 ± 0.16	0.42 ± 0.16
-0.60 - -0.40	0.44 ± 0.13	0.27 ± 0.09	0.15 ± 0.10	0.13 ± 0.12
-0.40 - -0.20	0.21 ± 0.10	0.17 ± 0.08	0.30 ± 0.09	0.25 ± 0.11
-0.20 - 0.00	0.17 ± 0.09	0.09 ± 0.07	0.14 ± 0.09	0.25 ± 0.10
0.00 - 0.20	0.25 ± 0.09	0.28 ± 0.08	0.22 ± 0.08	0.17 ± 0.11
0.20 - 0.40	0.48 ± 0.11	0.26 ± 0.08	0.42 ± 0.10	0.32 ± 0.12
0.40 - 0.60	0.45 ± 0.13	0.42 ± 0.10	0.42 ± 0.11	0.51 ± 0.15
0.60 - 0.80	1.02 ± 0.18	0.57 ± 0.13	0.77 ± 0.18	0.99 ± 0.24
0.80 - 1.00	1.76 ± 0.27	1.23 ± 0.20	1.86 ± 0.28	1.79 ± 0.33

Table 2. Differential cross-sections $d\sigma/d\Omega(\cos\theta_{\pi^0})$. There is a common systematic error of 16 %.

$\cos\theta_{\pi^0}$	$d\sigma/d\Omega(\cos\theta_{\pi^0})$ [$\mu\text{b}/\text{sr}$]	$d\sigma/d\Omega(\cos\theta_{\pi^0})$ [$\mu\text{b}/\text{sr}$]	$d\sigma/d\Omega(\cos\theta_{\pi^0})$ [$\mu\text{b}/\text{sr}$]	$d\sigma/d\Omega(\cos\theta_{\pi^0})$ [$\mu\text{b}/\text{sr}$]
E_γ [MeV]	1383 - 1817	1817 - 2020	2020 - 2256	2256 - 2382
-1.00 - -0.80	0.05 ± 0.03	0.23 ± 0.07	0.30 ± 0.07	0.40 ± 0.11
-0.80 - -0.60	0.05 ± 0.03	0.21 ± 0.05	0.32 ± 0.06	0.27 ± 0.09
-0.60 - -0.40	0.07 ± 0.03	0.09 ± 0.05	0.29 ± 0.06	0.40 ± 0.11
-0.40 - -0.20	0.04 ± 0.03	0.08 ± 0.05	0.27 ± 0.07	0.30 ± 0.11
-0.20 - 0.00	-0.04 ± 0.03	0.17 ± 0.05	0.23 ± 0.06	0.42 ± 0.11
0.00 - 0.20	0.06 ± 0.03	0.17 ± 0.05	0.18 ± 0.06	0.17 ± 0.10
0.20 - 0.40	0.03 ± 0.03	0.11 ± 0.05	0.30 ± 0.06	0.40 ± 0.12
0.40 - 0.60	0.03 ± 0.03	0.16 ± 0.06	0.27 ± 0.07	0.32 ± 0.10
0.60 - 0.80	0.07 ± 0.04	0.18 ± 0.06	0.24 ± 0.07	0.33 ± 0.11
0.80 - 1.00	0.04 ± 0.04	0.18 ± 0.08	0.18 ± 0.10	0.64 ± 0.17
E_γ [MeV]	2382 - 2495	2495 - 2677	2677 - 2845	2845 - 2970
-1.00 - -0.80	0.59 ± 0.14	0.67 ± 0.11	0.67 ± 0.14	0.61 ± 0.17
-0.80 - -0.60	0.54 ± 0.12	0.29 ± 0.10	0.37 ± 0.10	0.50 ± 0.14
-0.60 - -0.40	0.57 ± 0.13	0.37 ± 0.10	0.26 ± 0.11	0.32 ± 0.12
-0.40 - -0.20	0.47 ± 0.13	0.31 ± 0.10	0.34 ± 0.12	0.23 ± 0.14
-0.20 - 0.00	0.58 ± 0.13	0.46 ± 0.10	0.64 ± 0.12	0.43 ± 0.13
0.00 - 0.20	0.22 ± 0.12	0.12 ± 0.09	0.42 ± 0.12	0.49 ± 0.13
0.20 - 0.40	0.65 ± 0.14	0.39 ± 0.10	0.61 ± 0.12	0.60 ± 0.14
0.40 - 0.60	0.28 ± 0.12	0.29 ± 0.10	0.37 ± 0.13	0.58 ± 0.15
0.60 - 0.80	0.39 ± 0.15	0.39 ± 0.11	0.24 ± 0.12	0.09 ± 0.16
0.80 - 1.00	0.56 ± 0.27	0.15 ± 0.21	0.26 ± 0.16	0.35 ± 0.26

From these differential distributions the total cross-section was obtained by integrating over function (5) from t_{\min} to t_{\max} .

3.3 Total cross-section

The total cross-section was determined in three different ways, by extrapolation and summation of the three types of differential cross sections, $d\sigma/d\Omega(\cos\theta_\omega)$, $d\sigma/d\Omega(\cos\theta_{\pi^0})$, and $d\sigma/dt(|t-t_{\min}|)$ as described above. Statistical errors of the total cross-sections were determined by error propagation. As final result, the mean value of the total cross-section and the mean statistical error are shown in Fig. 10 (left) as a function of the photon energy. The cross-section rises with increasing photon energy, i. e. with the available phase space.

A systematic uncertainty was derived from the spread of the three different determinations of the total cross-section, using data of Fig. 6, 7 and 8. A further error of 5.7% was assigned to the Monte Carlo reconstruction efficiency [30]. These contributions and the 15% normalisation error [27] were added in quadrature to yield the total systematic error shown in Fig. 10.

3.4 The $\Delta^+\omega$ contribution to $p\pi^0\omega$

Fig. 11 shows the differential cross-sections $d\sigma/dm(p\pi^0)$, which were used to disentangle the $\Delta^+\omega$ contribution to

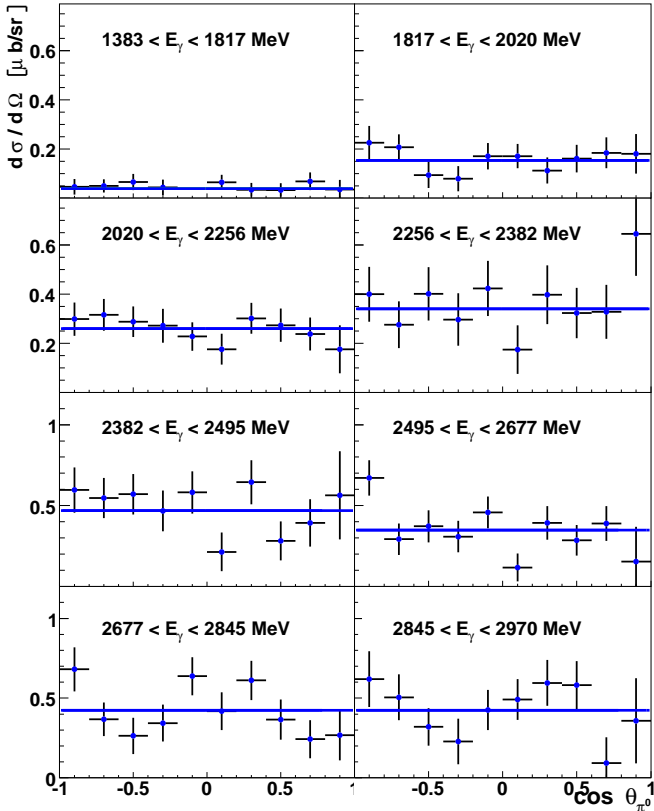


Fig. 7. Differential cross-sections $d\sigma/d\Omega(\cos\theta_{\pi^0})$.

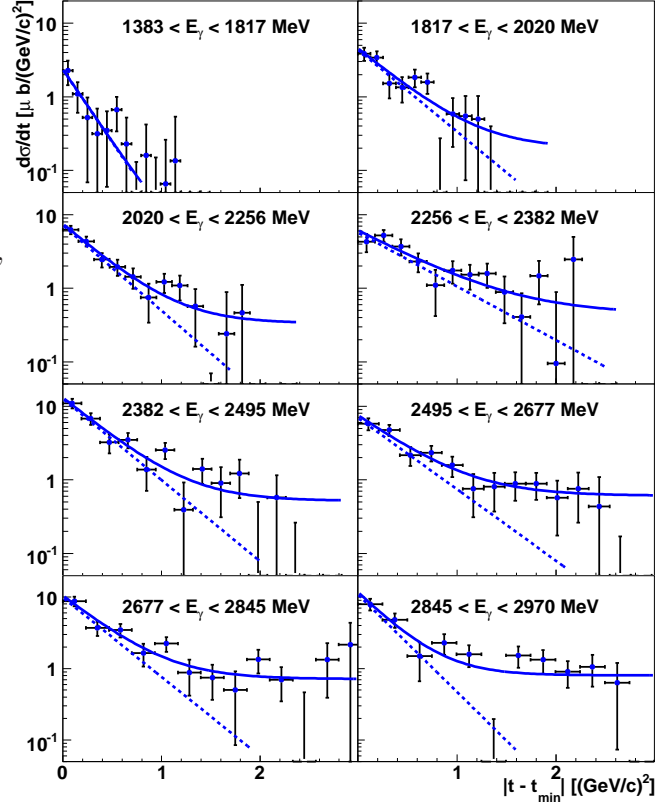


Fig. 8. Differential cross-sections $d\sigma/dt(|t-t_{\min}|)$ of the squared four-momentum transfer t to the $p\pi^0$ system.

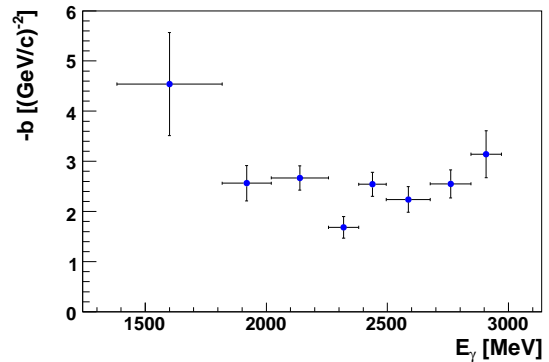


Fig. 9. Slope parameter of $d\sigma/dt(|t-t_{\min}|)$

the total cross-section. The distributions show prominent Δ signals. The Δ peak was fitted by a phase space corrected Breit-Wigner function (see e.g. [31] for details). The non-resonant $p\pi^0\omega$ part was described by phase-space distributed $p\pi^0\omega$ Monte Carlo events. Only the amplitudes of the two contributions were left free in the fit. The Breit-Wigner width of the Δ was fixed to $120 \text{ MeV}/c^2$ the mass was fixed to $1232 \text{ MeV}/c^2$ for energies below 2500 MeV and set to values between 1240 and $1250 \text{ MeV}/c^2$ for higher energies to improve the fit. With these two components a good description of the Δ peak and of the $p\pi^0\omega$

phase space contribution to the differential cross-section was achieved.

The Breit-Wigner distributions and the $p\pi^0\omega$ phase-space contributions were integrated and their fractions determined. The systematic uncertainty due to the disentanglement was estimated to 3 – 10% and added in quadrature to the systematic error. The cross-section for $\gamma p \rightarrow p\pi^0\omega$ without $\Delta^+\omega$ contributions is shown in Fig. 10 (right).

The total cross-section of $\gamma p \rightarrow \Delta^+\omega$ was determined from the observed fraction of $\Delta^+\omega$ events and the $\gamma p \rightarrow p\pi^0\omega$ cross-section, taking into account the unseen $\Delta^+ \rightarrow n\pi^+$ decay mode. The resulting cross-section is shown in Fig. 12 together with the results of the LAMP2 experiment [25]. It is worthwhile to discuss how the LAMP2 cross-section was determined.

The LAMP2 experiment measured the reaction $\gamma p \rightarrow \Delta^+\omega$ by identifying ω mesons in their $\pi^+\pi^-\pi^0$ decays. The Δ^+ decay products were not observed. Instead, the Δ^+ was identified in the missing mass spectrum of the $\gamma p \rightarrow \omega X$ reaction. The missing mass distribution (Fig. 13) contains signals for $p\omega$ and $\Delta^+\omega$ production. The authors give a 15% systematic uncertainty due to the difficulty in disentangling the $p\omega$, $p\pi^0\omega$ and $\Delta^+\omega$ contributions.

In our analysis the fraction of $p\pi^0$ below the Δ is significant (see fig. 11) and larger than estimated by LAMP2. Hence it seems possible that the LAMP2 cross-section is overestimated.

The total cross-section for $\Delta^+\omega$ photoproduction in Fig. 12 (see table 3) is consistent with a simple fit assuming a background amplitude in the form $A \cdot (E - E_{\text{threshold}})^{\alpha/2} \cdot (E - E_h)^{\beta/2}$ (A , α , β , $E_{\text{threshold}}$, E_h fit parameters). The $\chi^2 = 12.1$ for $N_{\text{DoF}} = 6$ corresponds to an acceptable 6% probability.

4 Summary

We have studied the reaction $\gamma p \rightarrow p\pi^0\omega$ with $\omega \rightarrow \pi^0\gamma$ from the $\omega\pi^0$ production threshold up to 3 GeV photon energy using an unpolarised tagged photon beam and a liquid hydrogen target. Differential cross-sections were determined as functions of $\cos\theta_\omega$, $\cos\theta_{\pi^0}$ and $|t - t_{\text{min}}|$. The distributions reveal strong contributions from isovector

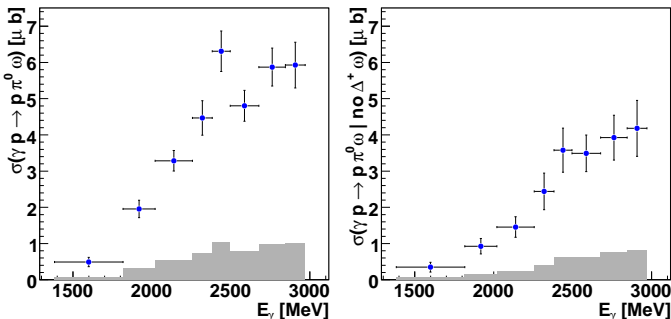


Fig. 10. Total cross-sections $\sigma(\gamma p \rightarrow p\pi^0\omega)$ before (left) and after (right) subtraction of the $\Delta^+\omega$ contribution. The grey band represents the systematic uncertainty.

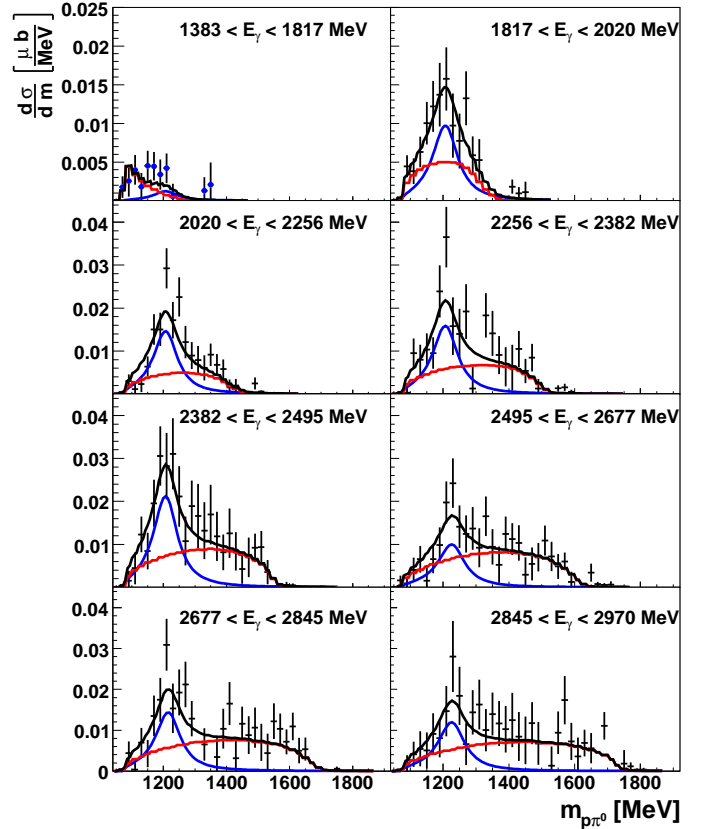


Fig. 11. Differential cross-sections $d\sigma/dm(p\pi^0)$. They are fitted with a combination of a Breit-Wigner (blue) and phase space $p\pi^0\omega$ Monte Carlo events (red).

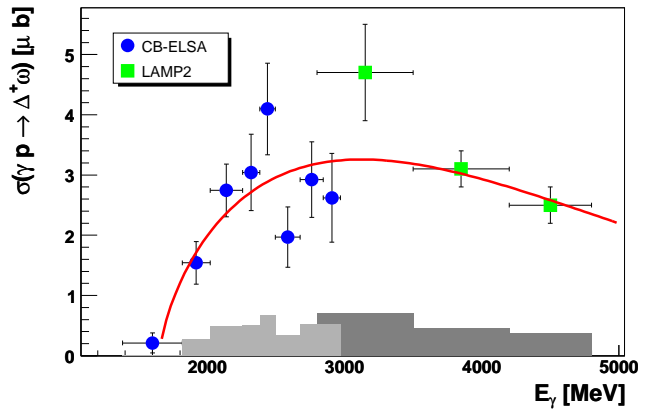


Fig. 12. Total cross-section $\sigma(\gamma p \rightarrow \Delta^+\omega)$, shown are the data from this analysis and from the LAMP2 experiment [25]. The systematic errors are shown as an error band in light (CB-ELSA) and dark grey (LAMP2). A fit to the data points is shown, which is described in the text.

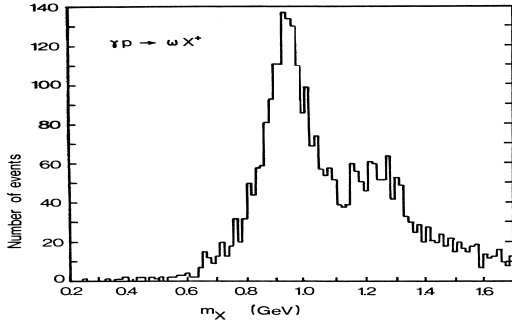


Fig. 13. Missing mass of the ω in the LAMP2 experiment (from [25]). Note that the spectrum is dominated by $p\omega$ events.

Table 3. Total cross-sections of $\gamma p \rightarrow p\pi^0\omega$ (with and without $\Delta^+\omega$ contribution) and $\gamma p \rightarrow \Delta^+\omega$. The systematic error is shown in Fig. 10 and 12.

E_γ [MeV]	$\sigma(\gamma p \rightarrow p\pi^0\omega)$ [μb]	$\sigma(\gamma p \rightarrow p\pi^0\omega)$ (no $\Delta^+\omega$) [μb]	$\sigma(\gamma p \rightarrow \Delta^+\omega)$ [μb]
1383 – 1817	0.49 ± 0.13	0.35 ± 0.13	0.21 ± 0.17
1817 – 2020	1.95 ± 0.24	0.93 ± 0.21	1.54 ± 0.35
2020 – 2256	3.28 ± 0.28	1.46 ± 0.28	2.74 ± 0.44
2256 – 2382	4.47 ± 0.47	2.44 ± 0.50	3.04 ± 0.63
2382 – 2495	6.31 ± 0.56	3.58 ± 0.61	4.10 ± 0.76
2495 – 2677	4.80 ± 0.43	3.49 ± 0.50	1.97 ± 0.50
2677 – 2845	5.87 ± 0.52	3.92 ± 0.62	2.92 ± 0.63
2845 – 2970	5.93 ± 0.63	4.18 ± 0.77	2.62 ± 0.74

exchange currents from the photon – converting to an ω meson – to the proton which undergoes a $p\text{-}\Delta$ excitation. The cross section for $\Delta\omega$ production and for non- $\Delta\omega$ events rises with increasing phase space; LAMP2 data indicate a decrease of the cross-sections when going to larger photon energies (3 - 5 GeV).

We thank the technical staff at ELSA and at all the participating institutions for their invaluable contributions to the success of the experiment. We acknowledge financial support from the Deutsche Forschungsgemeinschaft (DFG) within the Sonderforschungsbereich SFB/TR16. The collaboration with St. Petersburg received funds from DFG and the Russian Foundation for Basic Research. B. Krusche acknowledges support from Schweizerischer Nationalfond. U. Thoma thanks for an Emmy Noether grant from the DFG. A. V. Anisovich and A. V. Sarantsev acknowledge support from the Alexander von Humboldt Foundation. This work comprises part of the PhD thesis of J. Junkersfeld.

References

1. W.M. Yao *et al.*, J. Phys. G **33**, 1 (2006).
2. S. Capstick and N. Isgur, Phys. Rev. D **34** (1986) 2809.
S. Capstick and W. Roberts, Prog. Part. Nucl. Phys. **45** (2000) S241.

3. L. Y. Glozman, W. Plessas, K. Varga, and R. F. Wagenbrunn, Phys. Rev. D **58** (1998) 094030.
4. U. Löring, K. Kretzschmar, B. C. Metsch, and H. R. Petry, Eur. Phys. J. A **10** (2001) 309.
U. Löring, B. C. Metsch, and H. R. Petry, Eur. Phys. J. A **10** (2001) 395, 447
5. S. Capstick and W. Roberts, Phys. Rev. D **49** (1994) 4570.
6. S. Capstick, Phys. Rev. D **46** (1992) 2864.
7. S. Capstick and W. Roberts, Phys. Rev. D **58** (1998) 074011.
8. S. Capstick and W. Roberts, Phys. Rev. D **57** (1998) 4301.
9. A. V. Anisovich, A. Sarantsev, O. Bartholomy, E. Klempt, V. A. Nikonov and U. Thoma, Eur. Phys. J. A **25** (2005) 427.
A. Sarantsev, V. A. Nikonov, A. V. Anisovich, E. Klempt and U. Thoma, Eur. Phys. J. A **25** (2005) 441.
10. O. Bartholomy *et al.*, Phys. Rev. Lett. **94** (2005) 012003.
11. V. Crede *et al.*, Phys. Rev. Lett. **94** (2005) 012004.
12. B. Krusche *et al.*, Phys. Rev. Lett. **74** (1995) 3736.
13. O. Bartalini *et al.*, Eur. Phys. J. A **26** (2005) 399.
14. A. A. Belyaev *et al.*, Nucl. Phys. B **213** (1983) 201.
R. Beck *et al.*, Phys. Rev. Lett. **78** (1997) 606.
D. Rebreyend *et al.*, Nucl. Phys. A **663** (2000) 436.
15. J. Ajaka *et al.*, Phys. Rev. Lett. **81** (1998) 1797.
16. K.H. Althoff *et al.*, Z. Phys. C **18** (1983) 199.
E. J. Durwen, BONN-IR-80-7 (1980).
K. Buechler *et al.*, Nucl. Phys. A **570** (1994) 580.
17. R.A. Arndt *et al.*, W. J. Briscoe, I. I. Strakovsky, and R. L. Workman, <http://gwdac.phys.gwu.edu>.
18. K. H. Glander *et al.*, Eur. Phys. J. A **19** (2004) 251.
19. R. Lawall *et al.*, Eur. Phys. J. A **24** (2005) 275.
20. J. W. C. McNabb *et al.*, Phys. Rev. C **69** (2004) 042201.
21. B. Carnahan, UMI-31-09682 (microfiche), Ph.D. thesis (2003), CUA, Washington, D.C., see also R. Bradford *et al.*, Phys. Rev. C **73** (2006) 035202
22. R. G. T. Zegers *et al.*, Phys. Rev. Lett. **91** (2003) 092001.
23. J. Barth *et al.*, Eur. Phys. J. A **18** (2003) 117.
24. J. Ajaka *et al.*, Phys. Rev. Lett. **96** (2006) 132003.
25. D. P. Barber *et al.*, Z. Phys. C **26** (1984) 343.
26. W. Hillert, Eur. Phys. J. A **28S1** (2006) 139.
27. H. van Pee *et al.*, Eur. Phys. J. A **31** 61 (2007).
28. G. Suft *et al.*, Nucl. Instrum. Meth. A **538** (2005) 416.
29. E. Aker *et al.*, Nucl. Instrum. Meth. A **321** (1992) 69.
30. C. Amsler *et al.*, Z. Phys. C **58** (1993) 175.
31. A. V. Anisovich, A. Sarantsev, O. Bartholomy, E. Klempt, V. A. Nikonov and U. Thoma, Eur. Phys. J. A **25** (2005) 427.